Numerical Simulation of Hydraulic Jump with the Inclusion of Boussinesq Term

Wen Kiat Ting[1], How Tion Puay[1,*], Nor Azazi Zakaria[1]

[1] River Engineering and Urban Drainage Research Centre (REDAC), Universiti Sains Malaysia, Nibong Tebal, Pulau Pinang, Malaysia

ARTICLE INFO	ABSTRACT
	To design a hydraulic structure such as gravity dam, it is crucial to predict the. Location and the length of the hydraulic jump. Numerical model comes in handy to deal with the conditions which are costly to reproduce the laboratories such as the hydraulic jump experiment. In this study, two models (Saint-Venant model and Boussinesq model) are solved numerically to simulate the formation of hydraulic jump in a flat rectangular channel. The performance of the models in reproducing the flow profile of hydraulic jump and its location, under different advection solvers, i.e. the CIP, MUSCL, and upwind scheme are investigated. Numerical results showed that the inclusion of Boussinesq term does not have significant effect on the numerical reproduction of the hydraulic jump in terms of the location and the water surface gradient at the hydraulic jump. Numerical solutions show that the accuracy of the advection term solver and its shock-capturing capability is critical for accurate simulation of hydraulic jump.

1. Introduction

Hydraulic jump is a rapidly varied phenomenon in open channel flow. A hydraulic jump occurs when a supercritical upstream flow transited to a more tranquil subcritical downstream condition. At the location of hydraulic jump, water surface rises abruptly, surface rollers are formed, and energy is dissipated. Hydraulic jump is found at the outlet structure of gravity dam, stilling basin, downstream of bridge and culvert. It is one of the most effective mechanism to dissipate kinetic energy of flow into turbulent energy and potential energy. The purpose of energy dissipation is to protect the downstream riverbank and bed from erosion [1-5].

Hydraulic jump is classified into undular jump, weak jump, oscillating jump, steady jump, and strong jump based on the Froude number of the approaching flow, as shown in Figure 1. As the Froude number increases, the ratio of flow depth after hydraulic jump to before the jump increases, the amount of energy dissipated by the jump also increases [1,3].
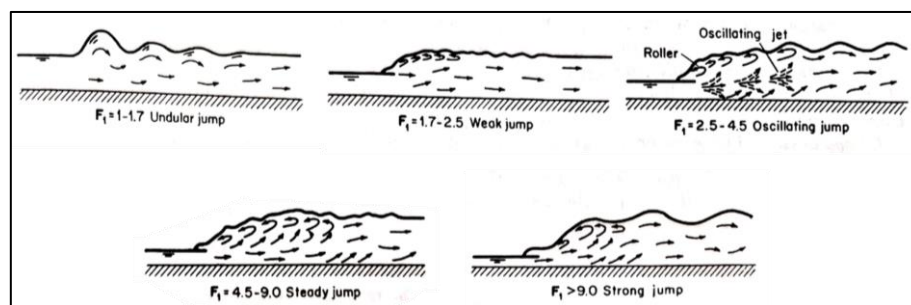

Fig. 1. Classification of hydraulic jump with Froude number [3]

Many experiments studies have been extensively investigated on the hydraulic jump in different roughness, i.e. hydraulic jump over smooth beds [6,7], and jump over rough beds [8,9]. By considering known flow depth and initial flow velocity, sequent depth ratio and the length of the jump can be determined using empirical or mathematical formula. It is undeniably that laboratory experiments provide actual flow characteristics by measurements, however it is too costly to conduct the experiments. With the advancement of computer technology, computational fluid dynamics (CFD) has been widely used in many fields such as heat transfer [23-26], hydrology, and hydraulic fields including the study of free-surface flow problems such as hydraulic jump.

A few numerical works have been done by the past researchers on the simulation of hydraulic jump using Boussinesq equations [10-12]. Chaudhry and Gharangik numerically simulated hydraulic jump by solving the Boussinesq equations using explicit finite difference schemes [10]. Raman and Chaudhry also solved the same problem using grid adaptation technique [11]. Pranab and Chaudhry simulated dam break flow by numerical solution of Boussinesq equations to investigate the effect of non-hydrostatic pressure distribution. The contribution of individual Boussinesq term was investigated by comparing the results of Saint-Venant equations and the Boussinesq equations [12]. In rapidly varied flow with steep water surface gradient, the pressure distribution is non-hydrostatic because of vertical acceleration. Therefore, the inclusion of Boussinesq term to account for the effect of non-hydrostatic pressure is required [10,11].

Constrained Interpolation Profile (CIP) scheme was developed by Yabe *et al.,* in 1985 [13]. It is a semi-Lagrangian scheme, which employed Lagrangian invariant solution $f(x_i, t + \Delta t) = f(x_i - u_i \Delta t, t)$, which always cast in non-conservative form [14]. The information in the grid cell, i.e. spatial derivatives and spatial gradients, are used to reconstruct a solution which are close to the real solution using cubic polynomial interpolation function [15]. CIP scheme is found to have third order accuracy in both time and space derivative [16]. CIP scheme has been proven to be superior as it can capture discontinuities without severe numerical oscillation. In other words, CIP possesses good shock-capturing capability. Similar work on the application of CIP scheme to solve the advection term in the governing equations for the simulation of hydraulic jump is not yet available at the point of writing. Therefore, this study is carried out to evaluate the performance CIP scheme in simulating hydraulic jump.

In this study, two numerical models are used to simulate the formation of hydraulic jump in a rectangular channel. The first model, namely Saint-Venant (SV) model solves the Saint-Venant equations and the second model, Boussinesq model solves the one-dimensional Boussinesq equations. Three different numerical schemes, i.e. Upwind, MUSCL and CIP schemes, are adopted to solve the advection term. The numerical simulations are coded in FORTRAN 95 programming language. The numerical results are compared with the experimental results by Chaudhry and Gharangik [10].

The Saint-Venant equations and the Boussinesq equations are nonlinear partial differential equations and the generalized analytical solution of these equations is not available. Besides that, Boussinesq term in the Boussinesq equations have third-order term and it is required to use third- or higher-order numerical methods to solve these equations [17]. Therefore, adoption of higher-order numerical scheme is required to solve the Boussinesq equations.

2. Methodology
2.1 Governing Equations

The Saint-Venant equations consist of the one-dimensional depth-averaged continuity and momentum equation as shown in Eq. (1) and Eq. (2a). The one-dimensional Boussinesq equations consist of the one-dimensional depth-averaged continuity equation and momentum equation with the inclusion of Boussinesq term as shown in Eq. (1) and Eq. (2b). The flow variables and the coordinate set up are defined Figure 2.

Continuity equation:
$$\frac{\partial h}{\partial t} + \frac{\partial (uh)}{\partial x} = 0 \tag{1}$$

Momentum equation:
$$\frac{\partial (uh)}{\partial t} + \frac{\partial (uuh)}{\partial x} = -gh\left(\frac{\partial h_s}{\partial x} + \frac{\tau_{bx}}{\rho g R}\right) \tag{2a}$$

Momentum equation with Boussinesq term included:
$$\frac{\partial (uh)}{\partial t} + \frac{\partial (uuh)}{\partial x} = -gh\left(\frac{\partial h_s}{\partial x} + \frac{\tau_{bx}}{\rho g R}\right) - \frac{\partial}{\partial x}(B_1 + B_2 + B_3) \tag{2b}$$

Here, u= depth-averaged velocity in x-direction, h_s= water surface elevation and h= flow depth. $A= Bh$ is the cross-sectional area of flow for rectangular channel where B is the width of the channel. τ_{bx}= bottom shear stress in x-direction, g= gravity acceleration, R= hydraulic radius and ρ = density of water, h_s is defined as $h_s = h\cos\theta + z_b$ with z_b = bed elevation measured from the datum. The Boussinesq terms, B_1, B_2 and B_3 in Eq. 2b account for the vertical acceleration and they are defined in Eq. (3) as follows:

$$B_1 = -\frac{h^3}{3}\left(\frac{\partial^2 u}{\partial x \partial t}\right) \qquad B_2 = -\frac{h^3}{3}\left(u\frac{\partial^2 u}{\partial x^2}\right) \qquad B_3 = \frac{h^3}{3}\left(\frac{\partial u}{\partial x}\right)^2 \tag{3}$$

The bottom shear stress term, τ_{bx} is evaluated in the model by using Manning's equation in Eq. (4) as follows,

$$\frac{\tau_{bx}}{\rho g R} = \frac{u|u|n^2}{h^{4/3}} \tag{4}$$

where n= Manning roughness coefficient. In deriving the relation in Eq. (4), the rectangular channel is assumed to be wide enough so that $R \approx h$.
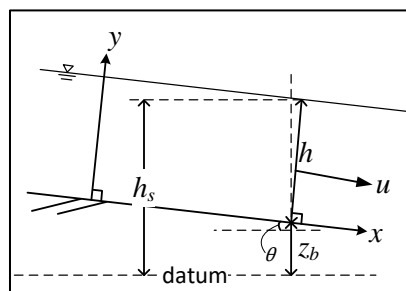
Fig. 2. Definition of flow variables in the governing equations

2.2 Numerical Solution

Three different numerical algorithms, each adopting different advection term solvers are used to solve the governing equations. The numerical algorithms are described as follows

i. Upwind + Adam-Bashforth (UP+AB)

The upwind scheme is used to evaluate the numerical fluxes in the advection term in both the continuity and momentum equations. The pressure, bottom shear stress and Boussinesq terms are discretized using finite difference method. The Adam-Bashforth multistep method is used to solve the time integration explicitly. This method is second order accurate in time and first-order accurate in space.

ii. MUSCL + Adam-Bashforth (MUSCL+AB)

The Monotonic Upstream-Centered Scheme for Conservation Laws (MUSCL scheme) is used to evaluate the momentum fluxes in the momentum equation. Meanwhile, upwind scheme is used to evaluate the mass fluxes (uh) in the continuity equation. The pressure, bottom shear stress and Boussinesq terms are discretized using finite difference method and the Adam-Bashforth multistep method is also used to solve the time integration explicitly. This method is of second-order accuracy in time and third-order accuracy in space.

iii. Constrained Interpolation Profile (CIP)

The Constrained Interpolation Profile (CIP) scheme is used to solve the advection term in both the continuity and momentum equations. The new flow depth and flow velocity are updated using the implicit SMAC method. The full algorithm for this method is explained in Section 2.3. This method is of third-order accuracy in both time and space.

For brevity, only the numerical algorithm for CIP scheme is explained in this manuscript. The algorithm for the upwind and MUSCL scheme are available in reference [18] and [19] respectively.

2.3 Solution Algorithm for CIP Solving Boussinesq Equation

The conservative form of the continuity and momentum equation in Eq. (1) and Eq. (2b) are changed into a non-conservative form as shown in Eq. (5) and Eq. (6). CIP scheme is used to solve the advection term on the left-hand side of Eq. (5) and Eq. (6).

$$\frac{\partial h}{\partial t} + u\frac{\partial h}{\partial x} = -h\frac{\partial u}{\partial x} \tag{5}$$

$$\frac{\partial u}{\partial t} + u\frac{\partial u}{\partial x} = -g\left(\frac{\partial}{\partial x}(h\cos\theta + z_b) + \frac{u|u|n^2}{h^{4/3}}\right) - \frac{1}{h}\frac{\partial}{\partial x}(B_1 + B_2 + B_3) \tag{6}$$

Time-splitting method [13] is used to solve Eq. (5) and Eq. (6) in two parts, i.e. the advection part (left-hand side) and the non-advection part (right-hand side).

Step 1

The advection part of the continuity and momentum equations are shown in Eq. (7) and Eq. (8). The value of h and u are upgraded to temporary values ($h*$ and $u*$) by using CIP scheme[13].

$$\frac{\partial h}{\partial t} + u\frac{\partial h}{\partial x} = 0 \xrightarrow{\text{solved with CIP}} \therefore h^n \rightarrow h^* \tag{7}$$

$$\frac{\partial u}{\partial t} + u\frac{\partial u}{\partial x} = 0 \xrightarrow{\text{solved with CIP}} \therefore u^n \rightarrow u^* \tag{8}$$

Step 2

After solving the advection term, the non-advection term can be solved by using Eq. (9) and Eq. (10) which are cast from Eq. (5) and Eq. (6).

$$\frac{\partial h}{\partial t} = -h\frac{\partial u}{\partial x} \tag{9}$$

$$\frac{\partial u}{\partial t} = -g\left(\frac{\partial}{\partial x}(h\cos\theta + z_b) + \frac{u|u|n^2}{h^{4/3}}\right) - \frac{1}{h}\frac{\partial}{\partial x}(B_1 + B_2 + B_3) \tag{10}$$

Eq. (9) and Eq. (10) can be discretized as Eq. (11) and Eq. (12) (based on staggered grid system shown in Figure 3).

$$\frac{h_i^{n+1} - h_i^*}{\Delta t} = -h_i^* \frac{u_{i+1}^{n+1} - u_i^{n+1}}{\Delta x} \tag{11}$$

$$\frac{u_i^{n+1} - u_i^*}{\Delta t} = -g\left(\frac{\partial h^{n+1}}{\partial x} + \frac{\partial(z_b)_i}{\partial x} + \frac{u^*|u^*|n^2}{(h^*)^{4/3}}\right) - \frac{1}{h^*}\frac{\partial}{\partial x}(B_1^* + B_2^* + B_3^*) \tag{12}$$

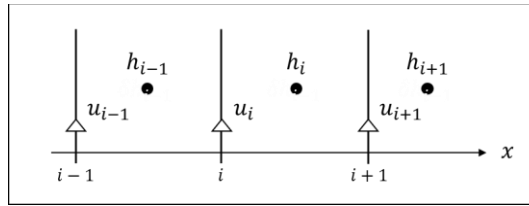**Fig. 3.** Staggered grid system used to define the location of flow variables used in the numerical model

where B_1^*, B_2^*, B_3^* are B_1, B_2, B_3 terms evaluated using temporary values h^* and u^* respectively. The calculation of new value h^{n+1} in Eq. (11) requires the new value u^{n+1}. However, as shown in Eq. (12), the calculation of u^{n+1} also requires the value of h^{n+1}. The implicit SMAC (Simplified Market and Cell) method [16] is used to solve for h^{n+1} and u^{n+1}. Based on Kawasaki *et al.,* [21], the implicit method SMAC method is described as follows.

First, an initial guess $\tilde{u}_i$ is calculated using Eq. (12) where all the terms on the right hand side of Eq. (12) are evaluated using h^* and u^* values as follows,

$$\tilde{u}_i = u_i^* - g\Delta t \left(\frac{\partial h_i^*}{\partial x} + \frac{\partial (z_b)_i}{\partial x} + \frac{u^*|u^*|n^2}{(h^*)^{4/3}} \right) - \frac{1}{h^*} \frac{\partial}{\partial x} (B_1^* + B_2^* + B_3^*) \tag{13}$$

Eq. (13) is then subtracted by Eq. (12), yielding the following relations:

$$\frac{u_i^{n+1} - \tilde{u}}{\Delta t} = -g \frac{\partial}{\partial x} (\delta h)_i \tag{14}$$

$$(\delta h)_i = h_i^{n+1} - h_i^* \tag{15}$$

Eq. (14) and Eq. (15) are then substituted into Eq. (11) to the following Poisson equation.

$$\frac{\partial^2 (\delta h)_i}{\partial x^2} = \frac{1}{g\Delta t} \left(\frac{\partial \tilde{u}}{\partial x} + \frac{(\delta h)_i}{\Delta t. h_i^*} \right) \tag{16}$$

The Poisson equation in Eq. (16) is discretized as follows,

$$\frac{\delta h_{i+1} + \delta h_{i-1} - 2\delta h_i}{(\Delta x)^2} = \frac{1}{g\Delta t} \left(\frac{\tilde{u}_{i+1} - \tilde{u}_i}{\Delta x} + \frac{(\delta h)_i}{\Delta t. h_i^*} \right) \tag{17}$$

$(\delta h)_i$ in Eq. (17) is solved with SOR (Successive Over Relaxation) method with the over-relaxation factor of 1.5.

Step 3

The new values of h and u are updated using Eq. (14) and Eq. (15), as shown in Eq. (18) and Eq. (19).

$$h_i^{n+1} = h_i^* + (\delta h)_i \tag{18}$$

$$u_i^{n+1} = \tilde{u}_i - g\Delta t \left(\frac{\delta h_i - \delta h_{i-1}}{\Delta x}\right) \tag{19}$$

2.4 Initial and Boundary Conditions

The initial condition is shown in Figure 4. At t = 0.0 s, the flow depth in the calculation domain is linearly interpolated using the inflow depth (h_{inlet}) and the outflow depth ($h_{outlet}/2$). The initial velocity u_i at each calculation cell is calculated in Eq. (20) where q is the discharge per unit width. q is evaluated using specified inlet velocity, u_{inlet} and specified inlet flow depth, h_{inlet} as shown in Eq. (21). u_{inlet} is calculated using the specified inflow Froude number Fr as shown in Eq. (22).

$$u_i = \frac{q}{h_i} \qquad\qquad \text{for } i = 2 \text{ to } i = ix \tag{20}$$

$$q = u_{inlet} \times h_{inlet} \tag{21}$$

$$u_{inlet} = Fr \times \sqrt{gh_{inlet}} \tag{22}$$

The inlet and outlet boundaries of the calculation domain are defined as the left side of cell $i = 1$ and right side of cell $i = ix + 1$ respectively as shown in Figure 4. The constant inflow discharge is used as the inlet boundary condition, as shown in Eq. (23).

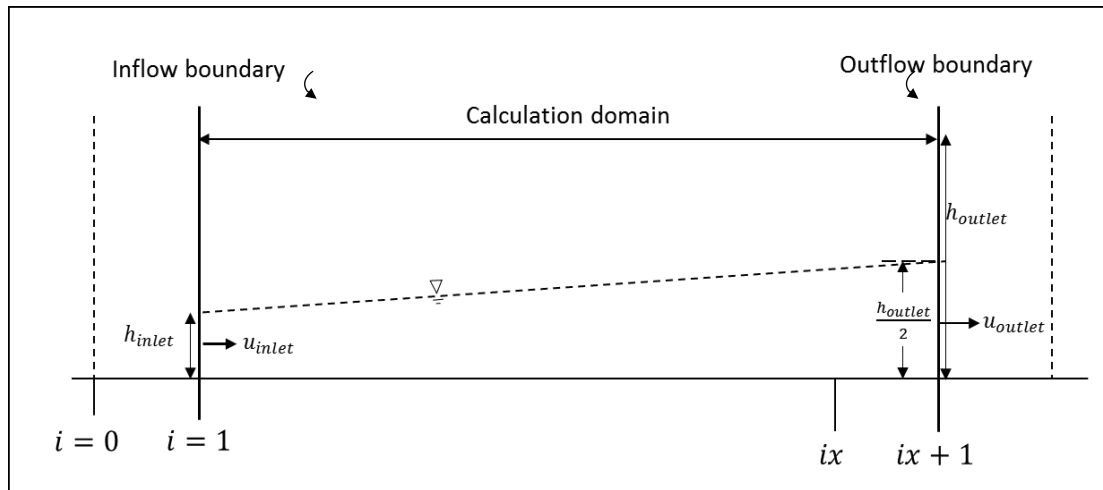$$h_{i=0} = h_{inlet}, \qquad u_{i=1} = u_{inlet} \tag{23}$$

Fig. 4. Initial condition and boundary condition used in the simulation of hydraulic jump

For the outlet boundary ($i = ix$), the outflow depth $h_{i=ix}$ is initially kept constant at $h_{i=ix} = h_{outlet}/2$ before being increased linearly with time from t= 10.0 s to t= 60.0 s. The outflow depth condition is summarized in Eq. (24). Meanwhile, a zero-velocity gradient condition (Eq. (25)) is applied at the last cell in the calculation domain.

$$h_{i=ix} = \begin{cases} \dfrac{h_{outlet}}{2}, & 0.0\ s < t \le 10.0\ s \\ \dfrac{h_{outlet}}{2} + \left(h_{outlet} - \dfrac{h_{outlet}}{2}\right) \times \dfrac{t}{60.0\ s}, & 10.0\ s < t \le 60.0\ s \\ h_{outlet}, & t > 60.0\ s \end{cases} \tag{24}$$

h_{outlet} = specified flow depth at the outflow boundary

$$\left.\frac{\partial u}{\partial x}\right|_{i=ix+1} = 0.0 \tag{25}$$

2.5 Mesh Convergence Test (MCT)

Mesh convergence test is carried out to determine the optimum mesh size by simulating one-dimensional hydraulic jump. Three different mesh sizes are used in the simulation using SV_(CIP) and the simulation results are compared with the experiment results. The parameters for the test are set up as shown in Table 1.

Table 1
Simulation conditions of hydraulic jump

Parameters	MCT 1	MCT 2	MCT3
Inflow Froude number, Fr		2.30	
Upstream flow depth, h_{inlet}		0.064 m	
Downstream flow depth, h_{outlet}		0.168 m	
Domain size (m)		9.60 m	
Time step, Δt (s)		1×10^{-4} s	
Cell size, Δx (m)	0.10 m	0.20 m	0.30 m

2.6 Simulation Condition

In the simulation, three hydraulic jump cases with different inflow Froude number (based on Chaudhry and Gharangik [10] experiment) are simulated. These three cases are used to reproduce the weak, oscillating and steady hydraulic jump. The simulation conditions are summarized in Table 2. Time step, $\Delta t = 1 \times 10^{-4}$ s and cell size, $\Delta x = 0.1$ m determined from the MCT are used in all the simulation cases.

Table 2
Simulation conditions of hydraulic jump

Inflow Froude number, Fr	Type of jump	Upstream flow depth, h_{inlet} (m)	Downstream flow depth, h_{outlet} (m)
2.30	Weak jump	0.064	0.168
4.23	Oscillating jump	0.043	0.222
5.74	Steady jump	0.040	0.286

The mixed time-space derivative of Boussinesq term, B_1 is ignored in the computations since it should be zero when a steady state is reached. Explicit artificial viscosity is introduced in the numerical algorithm with higher-order numerical scheme, i.e. MUSCL+AB and CIP to suppress the numerical oscillation and smoothen the variables (h and u) at the end of every time step [22]. Courant ratio at every calculation cell is calculated using Eq. (26) in every run to make sure that the Courant-Friedrichs-Lewy (CFL) condition is satisfied in the simulation [19].

$$Courant\ ratio = \frac{u\Delta t}{\Delta x} \qquad\qquad (26)$$

The Saint Venant (SV) and the Boussinesq (B) models are solved using three different advection term solvers, i.e. the UP+AB, MUSCL+AB and CIP, under three different inflow Froude number as shown in Table 3. The Manning's coefficient, n was determined by trial-and-error method by matching the water surface profile between the numerical and experimental result. Therefore, Manning's coefficient, n functioned as a calibration method to determine the location of hydraulic jump. The values of n varies from 0.013 to 0.022. The Manning's coefficient, n used in the simulation are summarized in Table 3.

Table 3
Manning's coefficient, n used in the numerical models

Inflow Froude number, Fr	Manning's coefficient, n		
	SV_(UP+AB)[1] B_(UP+AB)	SV_(MUSCL+AB) B_(MUSCL+AB)	SV_(CIP) B_(CIP)
2.30	0.013	0.013	0.016
4.23	0.020	0.020	0.022
5.74	0.020	0.020	0.022

Note (1): SV = Saint Venant model, B= Boussinesq model

The performance of the numerical model is evaluated by determine the relative error of the flow depth. The relative error is calculated using Eq. (27) as shown, by comparing the flow depth in the simulation results with the experimental result. The relative error of the flow depth at every point are first calculated and then the average values are recorded.

$$RE_h = \left|\frac{h_{sim} - h_{exp}}{h_{exp}}\right| \qquad\qquad (27)$$

where RE_h is the relative error of the flow depth, h_{sim} is the flow depth obtained from the simulation result, and h_{exp} is the flow depth obtained from the experimental result.

3. Results and Discussion
3.1 Result of Mesh Convergence Test

Figure 5 show the numerical results of water surface profile using 3 different mesh sizes, i.e., Δx= 0.1 m, 0.2 m, and 0.3 m. The relative error of the flow depth for MCT1, MCT2 and MCT3 against the experimental results are 0.99%, 3.40 % and 5.95% respectively. MCT1 (Δx= 0.1 m) has the lowest relative error as compared to MCT2 and MCT 3. MCT and MCT3 have higher discrepancy in term of the location and water surface gradient of the jump when compared with the experiment results. Hence, mesh size of Δx= 0.1 m is selected for the simulation of the one-dimensional hydraulic jump in the subsequent sections.
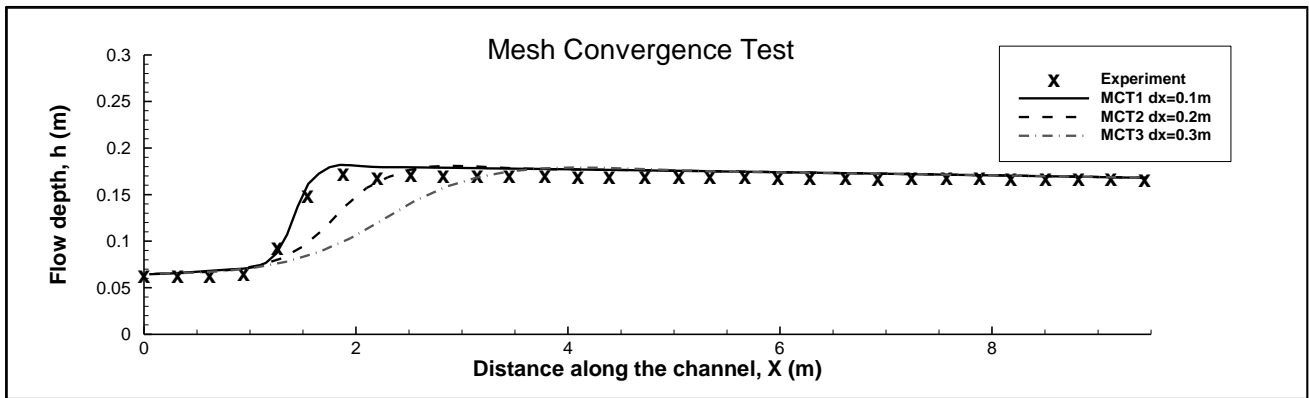
Fig. 5. Jump profile for Fr =2.3 at steady state (t= 120.0 s)

3.2 Formation of Hydraulic Jump

Figure 6 and Figure 7 show the numerical results of the water surface profile at different time lapse for B_(MUSCL+AB) and B_(CIP) respectively. The hydraulic jump started to form when the downstream depth was increased slowly. Subsequently, the jump travelled from the downstream end towards the upstream. The travel speed of the jump was reduced when the jump approached steady state. The jump remained steady at a fixed location at around t= 90.0 s. At steady state, the flow profile is smooth at the region away from the jump.
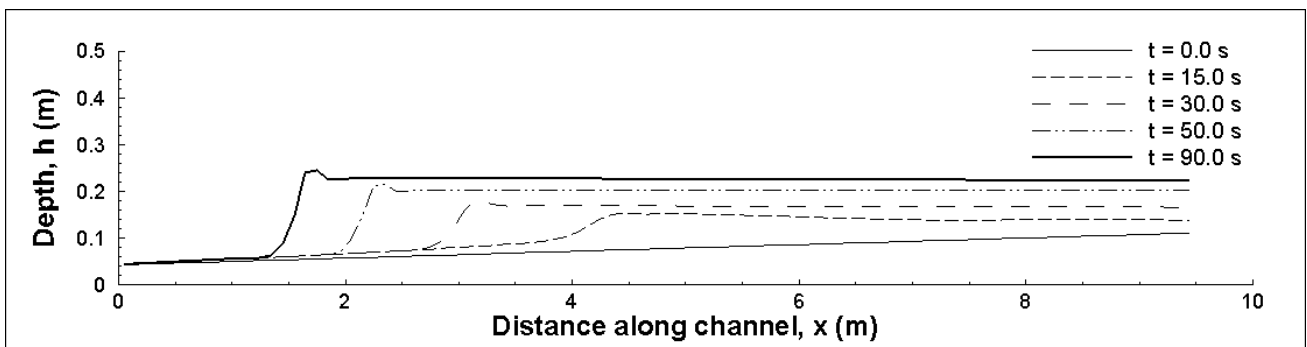

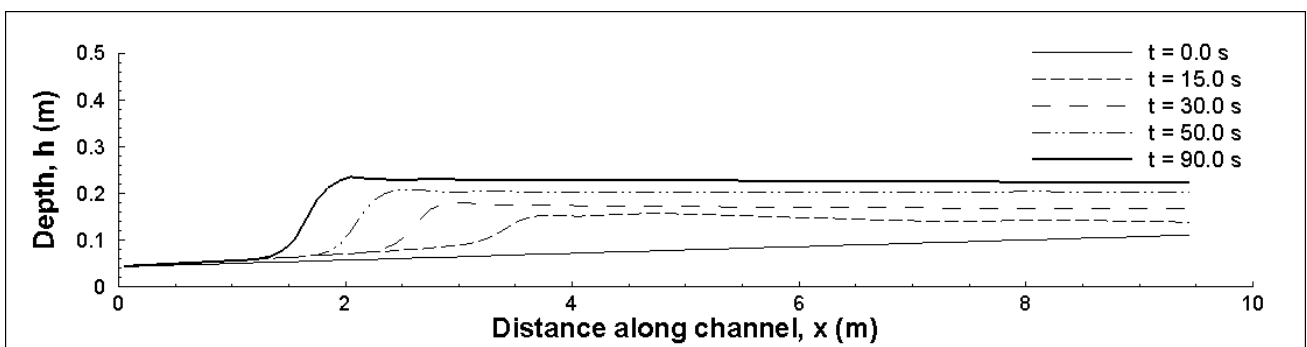**Fig. 6.** Water surface profile at different times for Fr =4.23 for B_(MUSCL+AB)

Fig. 7. Water surface profile at different times for Fr =4.23 for B_(CIP)

3.3 Steady-State Flow Profile

Figure 8 to Figure 10 show the comparison of steady-state flow profiles between the numerical and the experimental result while Table 3 show the relative error of the flow depth for every simulation cases. At the region away from the hydraulic jump, the flow profiles are smooth. This is because vertical acceleration is negligible in these regions and the pressure distribution is hydrostatic. Thus, all the models performed well in terms of the reproduction of the flow profile away from the hydraulic jump regardless of the inclusion of the Boussinesq term.

Numerical and experimental results showed that there was a sudden rise in flow depth at the location of hydraulic jump. This phenomenon is more evident in cases with higher inflow Froude number, i.e. at Fr =4.23 and Fr =5.74. Experimental observation reveals that at the hydraulic jump, flow is turbulent and vertical acceleration is non-negligible [10] and the pressure distribution at the hydraulic jump is non-hydrostatic.

As shown in Figure 8 to Figure 10 and Table 3, for all simulation cases, SV_(CIP) and B_(CIP) showed good agreement with the experimental result and all of their relative error are within 5.0%. It is evident that the gradient and the length of the hydraulic jump were well reproduced by SV_(CIP) and B_(CIP) as compared to the B_(UP+AB) and the B_(MUSCL+AB). B_(UP+AB) and B_(MUSCL+AB) showed acceptable results as all of their relative error of are within 10.0%, however the gradient of the jump was over predicted by the B_(UP+AB) and the B_(MUSCL+AB) as shown Figure 7 to Figure 9. In all simulation cases, the flow profiles generated by the SV_(UP+AB) and the SV_(MUSCL+AB) did not agree well with the experimental result in terms of the location of the jump and all of their relative errors exceeded 20.0%. In both models, the jumps are located nearer to the upstream end.

SV_(CIP) and B_(CIP) could reproduce approximately similar flow profiles in all cases. This shows that the inclusion of Boussinesq term in the B_(CIP) does not have significant effect on the numerical reproduction of the hydraulic jump in terms of the location and gradient of the hydraulic jump. Chaudhry and Gharangik [10] also concluded that Boussinesq term has little effect in determining the location of hydraulic jump in their numerical model.

On the contrary, comparison of the results between SV_(MUSCL+AB) and B_(MUSCL+AB), and between SV_(UP+AB) and B_(UP+AB) showed significant differences in terms of the location of hydraulic jump. Since Boussinesq term does not determined the location of the hydraulic jump, this shows that the MUSCL and Upwind scheme are much inferior in solving the advection terms in the continuity and momentum equations. Therefore, this implies that an accurate advection term solver with shock-capturing ability is critical in simulating hydraulic jump. Hence the application of CIP scheme, which is of third order accuracy and possesses shock-capturing ability, to solve the advection terms is well-justified.

Table 3
Relative error of the flow depth for different models and advection term solvers

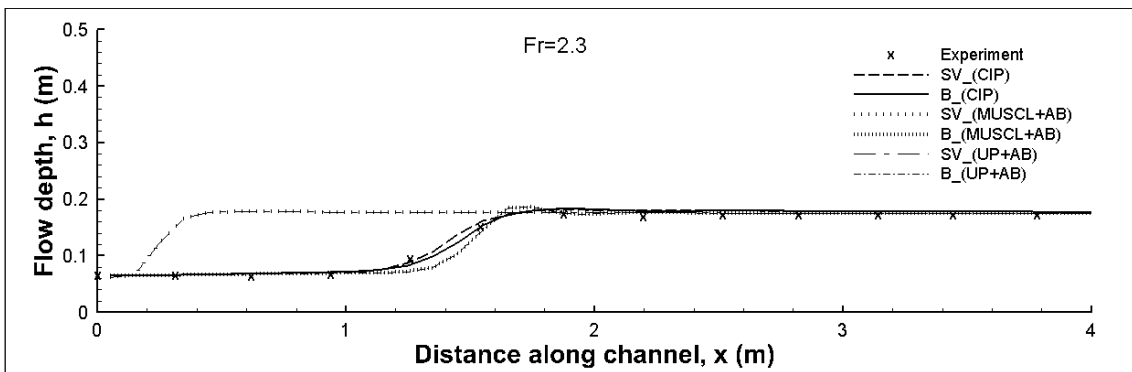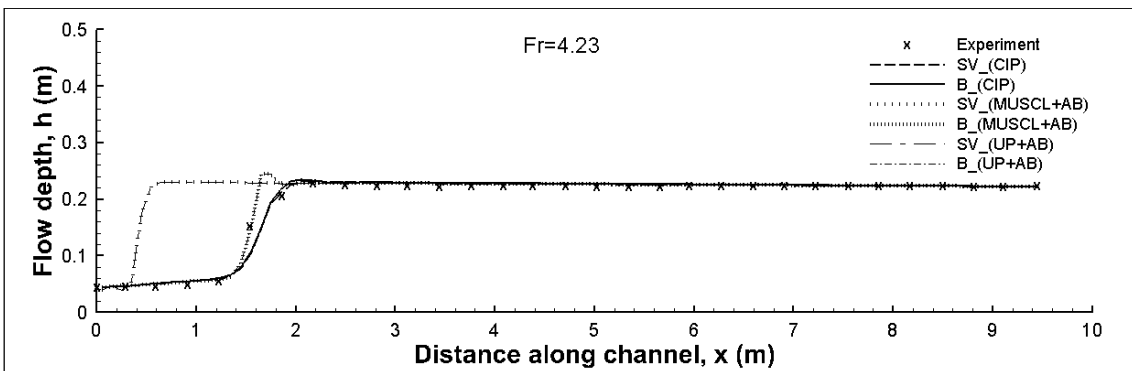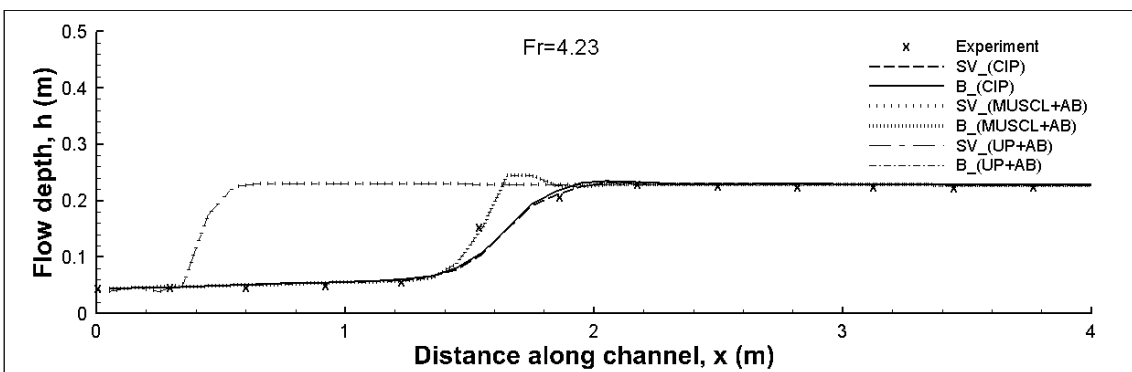| Inflow Froude number	Relative error (%)					
	SV_(Upwind+AB)	B_(Upwind+AB)	SV_(MUSCL+AB)	B_(MUSCL+AB)	SV_(CIP)	B_(CIP)
2.30	20.28	1.83	20.28	1.84	0.99	1.07
4.23	39.20	2.43	39.21	2.43	3.60	3.66
5.74	75.19	5.55	78.87	5.55	4.09	4.09

Note (1): SV = Saint Venant model, B= Boussinesq model
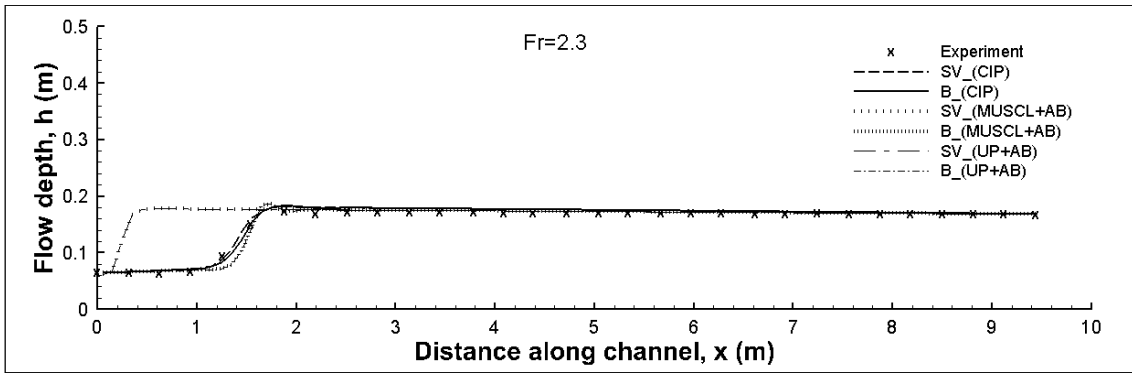
Fig. 8. Flow profile for Fr =2.3 at steady state (t= 120.0 s) (a) full domain view (b) close-up view at the jump

Fig. 9. Flow profile for Fr =4.23 at steady state (t= 120.0 s) (a) full domain view (b) close-up view at the jump
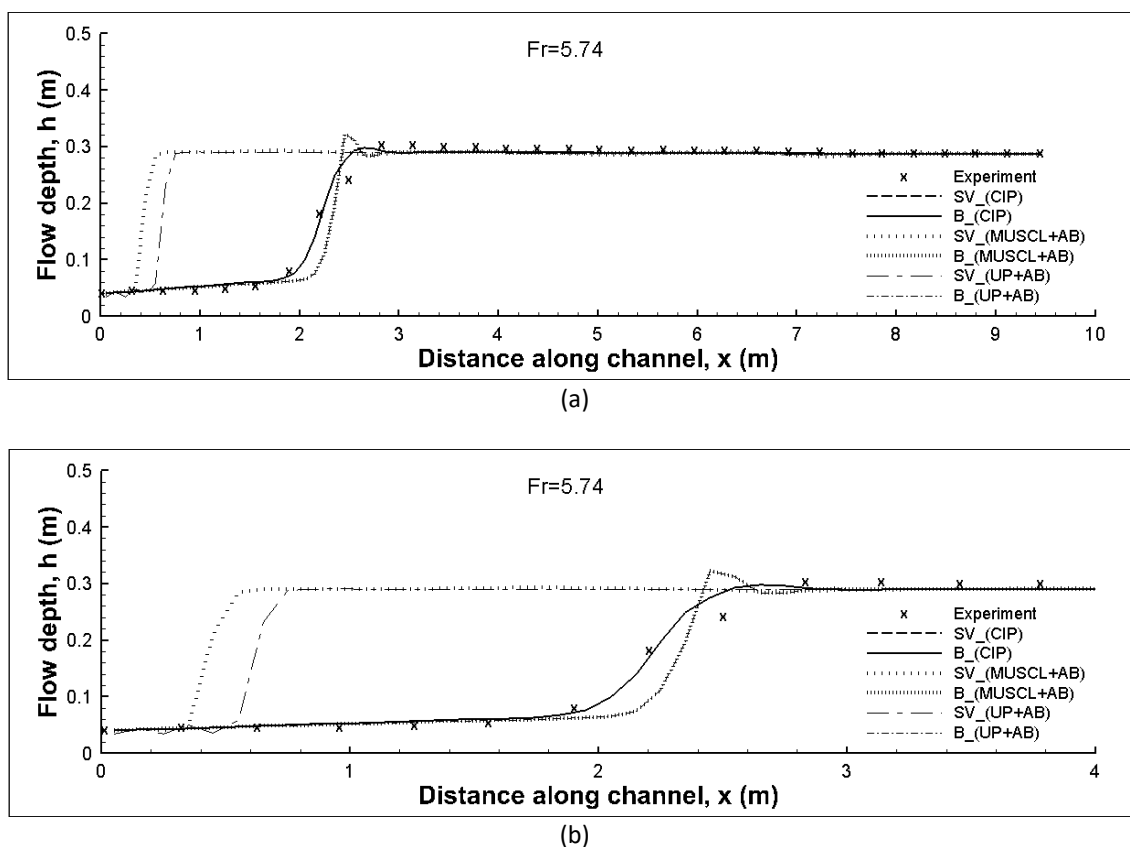
Fig. 10. Flow profile for Fr =5.74 at steady state (t= 120.0 s) (a) full domain view (b) close-up view at the jump

4. Conclusions

In this study, Saint-Venant model and Boussinesq model were solved numerically to simulate the formation of hydraulic jump in a flat rectangular channel. With appropriate initial and boundary conditions, numerical simulations were carried out until a final steady state was reached.

Numerical results showed that the inclusion of Boussinesq term does not have significant effect on the numerical reproduction of the hydraulic jump in terms of the location and the water surface gradient at the hydraulic jump. Numerical solutions showed that the accuracy of the advection term solver and the ability of the scheme to capture shock is critical in simulating hydraulic jump. Hence, a numerical scheme with accurate advection term solver is required in the simulation of the phenomena of shock wave.

References

[1] Chanson, Hubert. "The Hydraulics of Open Channel Flow: An Introduction." London: Elsevier Butterworth-Heinemann (2004). https://doi.org/10.1016/B978-075065978-9/50006-4

[2] Chaudry, M. Hanif. *Open-Channel Flow*. Columbia: Springer, 2008. https://doi.org/10.1007/978-0-387-68648-6

[3] Chow, Ven T. "Open-channel hydraulics." *McGraw-Hill civil engineering series* (1959).

[4] Hager, Willi H. *Energy dissipators and hydraulic jump*. The Netherlands: Kluwer Academic Publishers, 1992. https://doi.org/10.1007/978-94-015-8048-9

[5] Osman Akan, A. *Open Channel Hydraulics*. Elsevier, Oxford, UK, 2006. https://doi.org/10.1016/B978-075066857-6/50008-4

[6] Rajaratnam, Nallamuthu. "The hydraulic jump as a well jet." *Journal of the Hydraulics Division* 91, no. 5 (1965): 107-132. https://doi.org/10.1061/JYCEAJ.0001299

[7]   Mortazavi, Milad, Vincent Le Chenadec, Parviz Moin, and Ali Mani. "Direct numerical simulation of a turbulent hydraulic jump: turbulence statistics and air entrainment." *Journal of Fluid Mechanics* 797 (2016): 60-94. https://doi.org/10.1017/jfm.2016.230

[8]   Rajaratnam, N. "Hydraulic jumps on rough beds." *Trans. Eng. Inst. Canada* 11, no. A-2 (1968): 1-8.

[9]   Hager, Willi H. "Classical Hydraulic Jump." *In: Energy dissipators and hydraulic jump.* Springer, Dordrecht, Netherlands (2013): 5–40. https://doi.org/10.1007/978-94-015-8048-9_2

[10]   Gharangik, Araz M., and M. Hanif Chaudhry. "Numerical simulation of hydraulic jump." *Journal of hydraulic engineering* 117, no. 9 (1991): 1195-1211. https://doi.org/10.1061/(ASCE)0733-9429(1991)117:9(1195)

[11]   Rahman, Mizanur, and M. Hanif Chaudry. "Simulation of hydraulic jump with grid adaptation." *Journal of Hydraulic Research* 33, no. 4 (1995): 555-569. https://doi.org/10.1080/00221689509498660

[12]   Mohapatra, Pranab K., and M. Hanif Chaudhry. "Numerical solution of Boussinesq equations to simulate dam-break flows." *Journal of Hydraulic Engineering* 130, no. 2 (2004): 156-159. https://doi.org/10.1061/(ASCE)0733-9429(2004)130:2(156)

[13]   Takewaki, Hrn, A. Nishiguchi, and T. Yabe. "Cubic interpolated pseudo-particle method (CIP) for solving hyperbolic-type equations." *Journal of computational physics* 61, no. 2 (1985): 261-268. https://doi.org/10.1016/0021-9991(85)90085-3

[14]   Yabe, Takashi, Ryotaro Tanaka, Takashi Nakamura, and Feng Xiao. "An exactly conservative semi-Lagrangian scheme (CIP–CSL) in one dimension." *Monthly Weather Review* 129, no. 2 (2001): 332-344. https://doi.org/10.1175/1520-0493(2001)129%3C0332:AECSLS%3E2.0.CO;2

[15]   Yabe, Takashi, Feng Xiao, and Takayuki Utsumi. "The constrained interpolation profile method for multiphase analysis." *Journal of Computational physics* 169, no. 2 (2001): 556-593. https://doi.org/10.1006/jcph.2000.6625

[16]   Yabe, Takashi, Hiroki Mizoe, Kenji Takizawa, Hiroshi Moriki, Hyo-Nam Im, and Youichi Ogata. "Higher-order schemes with CIP method and adaptive Soroban grid towards mesh-free scheme." *Journal of Computational Physics* 194, no. 1 (2004): 57-77. https://doi.org/10.1016/j.jcp.2003.08.019

[17]   Abbott, M. B., McCowan, A., and Warren, I. R. "Improved simulations of wave propagation. " IAHR 7 (Sep.), (1983): 78-81.

[18]   Tion, Puay How, Lim Jia Jun, and Nor Azazi Zakaria. "Numerical simulation of mudflow with a two-dimensional depth-averaged model." *Jurnal Teknologi* 83, no. 3 (2021): 1-10. https://doi.org/10.11113/jurnalteknologi.v83.14069

[19]   Pletcher, Richard H., John C. Tannehill, and Dale Anderson. *Computational fluid mechanics and heat transfer 3rd edition.* 2012.

[20]   Amsden, Anthony A., and Francis H. Harlow. "A simplified MAC technique for incompressible fluid flow calculations." *Journal of computational physics* 6, no. 2 (1970): 322-325. https://doi.org/10.1016/0021-9991(70)90029-X

[21]   KAWASAKI, Koji, Toshikazu ONO, Napaporn PIAMSA-NGA, Hiroshi ATSUTA, and Keiji NAKATSUJI. "Development of depth-averaged inundation flow model based on CIP method and SMAC method." *Proceedings of Hydraulic Engineering* 48 (2004): 565-570. https://doi.org/10.2208/prohe.48.565

[22]   Jameson, Antony, Wolfgang Schmidt, and Eli Turkel. "Numerical solution of the Euler equations by finite volume methods using Runge Kutta time stepping schemes." In *14th fluid and plasma dynamics conference*, p. 1259. 1981. https://doi.org/10.2514/6.1981-1259

[23]   Fekadu, Birlie, and H. V. Harish. "Numerical Studies on Thermo-Hydraulic Characteristics of Turbulent Flow in a Tube with a Regularly Spaced Dimple on Twisted Tape." *CFD Letters* 13, no. 8 (2021): 20-31. https://doi.org/10.37934/cfdl.13.8.2031

[24]   Rosly, Nurhayati, Qamarul Ezani Kamarudin, and Bambang Basuno. "Comparative Study on Various Numerical Schemes for Solving Nozzle Flow Problems." *CFD Letters* 12, no. 6 (2021): 93–106. https://doi.org/10.37934/cfdl.13.8.2031

[25]   Mostafa, Nabil H., and Mohamed Adel. "Unsteady numerical simulation of cavitation in axial turbine." CFD Letters 4, no. 3 (2021): 140–149.

[26]   Ewis, Karem Mahmoud. "Effects of Variable Thermal Conductivity and Grashof Number on Non-Darcian Natural Convection Flow of Viscoelastic Fluids with Non Linear Radiation and Dissipations." *Journal of Advanced Research in Applied Sciences and Engineering Technology* 22, no. 1 (2021): 69-80.